



**HAL**  
open science

# Electro-mechanical Resonant Ice Protection Systems: Power requirements for fractures initiation and propagation

Valerian Palanque, Marc Budinger, Valerie Pommier-Budinger, Lokman  
Bennani, David Delsart

► **To cite this version:**

Valerian Palanque, Marc Budinger, Valerie Pommier-Budinger, Lokman Bennani, David Delsart. Electro-mechanical Resonant Ice Protection Systems: Power requirements for fractures initiation and propagation. AIAA Aviation 2021 Forum, Aug 2021, VIRTUAL EVENT, United States. pp.AIAA 2021-2651, 10.2514/6.2021-2651 . hal-03414409

**HAL Id: hal-03414409**

**<https://hal.science/hal-03414409>**

Submitted on 4 Nov 2021

**HAL** is a multi-disciplinary open access archive for the deposit and dissemination of scientific research documents, whether they are published or not. The documents may come from teaching and research institutions in France or abroad, or from public or private research centers.

L'archive ouverte pluridisciplinaire **HAL**, est destinée au dépôt et à la diffusion de documents scientifiques de niveau recherche, publiés ou non, émanant des établissements d'enseignement et de recherche français ou étrangers, des laboratoires publics ou privés.

# Electromechanical Resonant Ice Protection Systems: Power requirements for fractures initiation and propagation

Valerian Palanque

*ISAE SUPAERO and ONERA/DMPE, University of Toulouse, F-31055 Toulouse - France*

Marc Budinger

*Institut Clément Ader (ICA), University of Toulouse, INSA, ISAE-SUPAERO, MINES ALBI, UPS, CNRS*

Valérie Pommier-Budinger

*ISAE SUPAERO, University of Toulouse, France*

Lokman Bennani

*ONERA/DMPE, University of Toulouse, F-31055 Toulouse - France*

David Delsart

*ONERA/DMAS, F-59045 Lille - France*

**This article focuses on resonant ice protection systems and studies fracture mechanisms at work for flexural modes having frequencies lower than 100 kHz. The objective is to study the power required for fracture initiation and propagation in this frequency range. Two types of deicing mechanisms are studied in this paper: tensile stress dominant flexural modes and shear stress dominant flexural modes. Criteria are introduced to enable the comparison between these deicing mechanisms according to their power requirements and the selection of the most promising configurations. Eventually, the numerical results are compared to experiments to verify assumptions and computations. The contribution of this article is to put forward power-efficient de-icing configurations for resonant electromechanical de-icing systems using flexural modes. Low frequency flexural modes appear to be less power consuming for both mechanisms. Tensile stress dominant flexural modes have lower power requirements than shear stress dominant modes. The instantaneous peak power requirement to cover 90% of the area is estimated to be 5.5 kW/m<sup>2</sup>.**

## Nomenclature

$A$	=	Area (m <sup>2</sup> )
$b$	=	Fracture width (m)
$C_{shear}$	=	Criterion for fracture initiation by shear stress
$C_{tensile}$	=	Criterion for fracture initiation by tensile stress
$C_{coh}$	=	Criterion for cohesive fracture unstable propagation

$C_{adh}$	=	Criterion for adhesive fracture unstable propagation
$F$	=	Force (N)
$G$	=	Energy release rate (J/m <sup>2</sup> )
$G_c$	=	Critical energy release rate (J/m <sup>2</sup> )
$K_{eq}$	=	Equivalent stiffness of the mass-stiffness system (N/m)
$l_f$	=	Fracture length (m)
$M_{eq}$	=	Equivalent mass of the mass-stiffness system (kg)
$\omega$	=	Angular frequency (rad/s)
$P$	=	Power per area (W/m <sup>2</sup> )
$Q_m$	=	Quality factor (-)
$\sigma$	=	Stress (Pa)
$\sigma_{adm}$	=	Material allowable tensile stress (Pa)
$\tau_{adm}$	=	Material allowable shear stress (Pa)
$\tau_{mod}$	=	Modal shear stress (Pa)
$\sigma_{mod}$	=	Modal tensile stress (Pa)
$U$	=	Strain energy per area (J/m <sup>2</sup> )
$x$	=	Vibratory amplitude (m)

## I. Introduction

According to Gent et al [1], aircraft icing occurs during flight in clouds at temperatures at or below water freezing point. Super-cooled water droplets reach and freeze on unprotected areas on which they impact (hence the term “impact icing” used in the BS 3G100 icing requirements [2]). The ice build-ups on airfoils can lead to significant aerodynamic disturbances, increasing drag and reducing lift. Eventually, under strong icing conditions, ice will grow enough to threaten downstream parts of the airplane, in case of massive uncontrolled shedding. According to the EASA CS-25 document [3], the aircraft can encounter various different “maximum icing” conditions which occurs in atmospheric icing conditions. Authorities require either to prevent leading edges from icing or to remove the ice before a critical amount accretes. It must be demonstrated that the full range of atmospheric icing conditions have been considered. Effective ice protection systems are therefore required to enable aircraft certification, at the cost of significant consumption. Bleed air anti-icing systems are aircraft second largest energy consumers among non-propulsive systems [4]. Electro-thermal solutions remain highly energy consuming. Pneumatic boot and electro-impulse technologies, based on mechanical principle, consume less energy but on the other hand, tend to have shorter life cycles and bulkier power supplies. The objective of this paper is to pursue previous works concerning resonant electromechanical de-icing systems, in order to propose low consumption and light solutions for ice protection systems. The principle of such devices is to apply vibrations to the protected area which exceed the mechanical allowable properties of ice. Thanks to resonant phenomenon, it is possible to reach higher amplitudes and therefore higher stresses values for a given power input.

A wide range of frequencies has been studied so far. Ramanathan et al.[5], studied piezoelectric application at very high frequencies (Over 1 MHz). They assumed that the shear strength of the ice was over 1.38 MPa and computed the displacement required to create such a stress at the interface. Venna et al. [6] studied the use of piezoelectric actuators at a much lower frequency (around 1 kHz). The objective was to use two sets of electrodes to generate both shear and normal stresses. Palacios et al. [7] mainly studied the application of ultrasonic range frequencies (around 20 kHz or more) working on instantaneous de-icing.

Looking closer at the mode shapes, Pommier-Budinger et al. [8] divided eigenmodes in two categories: extensional modes and flexural modes. It was found out that extensional modes exist at higher frequency than flexural modes, and tend to better delaminate ice, whereas flexural modes are more likely to initiate cracks in a cohesive way. The paper also shows that the crack initiation requires less energy for low frequencies flexural modes. This paper focuses only on flexural modes, and tends to go further in their study by extending the frequency range up to 100 kHz.

According to these studies, the resonant phenomenon seems to give hopeful results for energetic consumption as shown by Palacios et al. [7], giving a mean power requirement over a 100 times inferior to conventional electric heat de-icing system. The piezoelectric actuators appear to be well adapted for this type of application, with its natural integration on airfoil as shown in previous works [6]–[8], and their capacity to generate excitation over a broad range of frequency and for different types of resonant modes. Similar experimental studies were made by Villeneuve et al. to show capability of fracture initiation and propagation using piezoelectric ceramics to actuate low frequency flexural

modes [9]–[11]. This article focuses on modes having frequencies under 100 kHz. The objective of this paper is to quantify power requirements to either initiate or propagate cracks on ice layers with such modes. In section II, criteria are introduced to help comparing modes over the whole frequency range. Section III presents the computations of the criteria for initiating fractures and Section IV gives the criteria for propagating fractures. Section V proposes a synthesis to highlight advantages and drawbacks of each type of mode and the selection of the most power-efficient de-icing strategies. In Section VI, cases representing these promising strategies are studied experimentally, which enables a verification of numerical hypotheses and computations.

## II. De-icing architecture system

In order to achieve mechanical de-icing, the idea is to vibrate the area to be protected using electromechanical actuators. The use of the phenomenon of resonance enables to reach high vibrating amplitudes with low amplitude actuation. Hence the energy and power requirements to bring the structure to the required vibration amplitude is lowered. In this paper, piezoelectric ceramics are used to excite the structure. Ceramic plates fit well on airfoil skin structures thanks to their natural shape. Figure 1 shows an example of a leading edge equipped with a piezoelectric de-icing set-up. In order to understand de-icing mechanisms, simplified beam and plate models are studied to focus on the fracture mechanisms of the ice. Figure 2 shows an example of the plate sample geometry studied in the paper. This article aims to define design criteria to help selecting eigenmodes and de-icing mechanisms according to their power consumption.

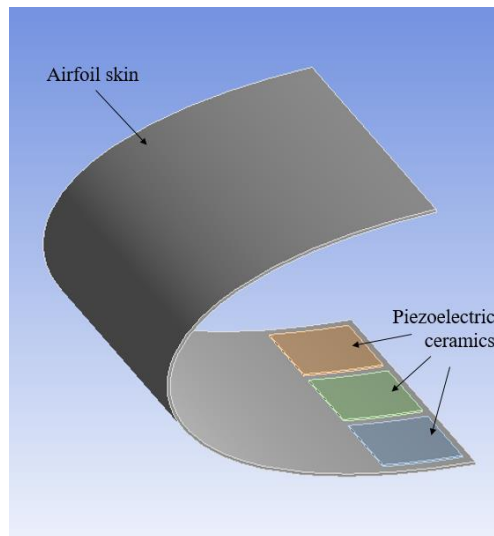


Figure 1 Airfoil equipped with piezoelectric ceramics

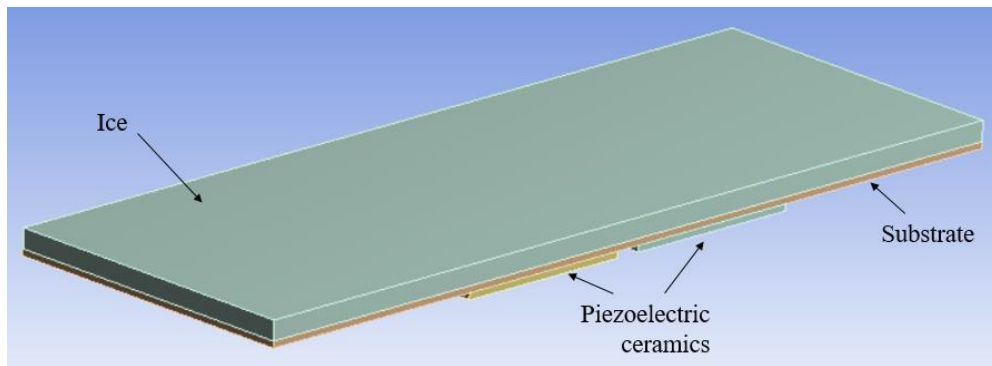


Figure 2 Plate sample equipped with piezoelectric ceramics

### III. Introduction to design criteria

#### A. Objectives

The idea behind the criteria comes from electric motor constants characteristics or similarity laws for turbomachinery constituted by ratios of magnitudes that evolve independently from the operating points [12]. The first objective of the article is to define criteria allowing:

- To compare different modes and different de-icing mechanisms
- To express results in a synthetic and quantifiable way from finite element simulations.
- To be free from the operating point and its vibratory amplitude.
- To have results independent from some non-geometric variables.
- To assess power requirements for given configurations/modes.

The final objective of the article is to combine these criteria to help selecting configurations of resonant electromechanical de-icing systems and designing low-power ice protection systems.

#### B. Modeling principles and criteria introduction

It is of prior interest to be capable of assessing the required power to initiate fractures and then propagate them. The methodology used in this article is based on the modal analysis of various resonant modes identified for de-icing purposes. A common way to perform vibrating finite element analysis is by using harmonic responses. However, harmonic responses analyses are usually coupled with modal analyses, therefore settle results with only modal analyses spares consequent computation time. Modal analysis allows running simulations without having to manage with loading conditions and damping coefficients. Modal results are readily rescaled in post-processing phases and thus more adjustable when it comes to confrontation with experiments.

This article focuses only on pure flexural modes. For this type of mode, the displacement is assumed to be unidirectional which allows establishing for each mode an equivalent damped spring-mass system: the mass being  $M_{eq}$ , the stiffness  $K_{eq}$ , and the damping ratio being expressed through its quality factor  $Q_m$ .

The strain energy density  $U$  is proportional to the vibratory amplitude  $x$  squared:

$$U = \frac{1}{A} \left( \frac{1}{2} \cdot K_{eq} \cdot x^2 \right) \rightarrow U \propto x^2 \quad (1)$$

With  $A$  the surface area of the plate model under study.  
The stress  $\sigma$  is proportional to the vibratory amplitude  $x$ :

$$\sigma \propto x \quad (2)$$

The force amplitude  $F$  required by such vibratory amplitude  $x$  is given at resonance frequency by:

$$F = \frac{K_{eq} x}{Q_m} \quad (3)$$

The associated mechanical power per area  $P$  is given by:

$$P = \frac{1}{A} \frac{1}{2} F \dot{x} = \frac{1}{A} \frac{1}{2} \frac{K_{eq} x^2 \omega}{Q_m} = \frac{U \omega}{Q_m} \quad (4)$$

For power computations, manipulated quantities represent the peak amplitudes of the sinusoidal values. The  $\frac{1}{2}$  ratio is used to compute the rms value of the power, which is more representative of the power requirement than the peak value.

Using these relations, analysis criteria are defined to link power per area with stresses in the ice, both in the ice itself and at its interface with the substrate. Another criterion is also defined as a ratio between the power per area and the energy release rate  $G$ , representing systems delamination effectiveness.

To explain the interest of the criteria, let us first treat the example of the criteria that link power and stress. To compute the power per area given by equation (4), the real strain energy is to be known. However, modal analysis only provides a modal energy. Modal values  $U_{mod}$ ,  $x_{mod}$  and  $\sigma_{mod}$  can be rescaled to get real values  $U_r$ ,  $x_r$  ... When the purpose is to study cohesive fracture initiation, the modal values are rescaled according to the ice tensile strength  $\sigma_{adm}$ . According to the previous hypotheses:

$$\frac{x_r}{x_{mod}} = \frac{\sigma_{adm}}{\sigma_{mod}} \quad \text{and} \quad \frac{U_r}{U_{mod}} = \frac{x_r^2}{x_{mod}^2} = \frac{\sigma_{adm}^2}{\sigma_{mod}^2} \quad (5)$$

Hence, the mechanical power per area can be expressed as function of the finite element modal values:

$$P_{mech} = \frac{U_{mod} \omega \sigma_{adm}^2}{\sigma_{mod}^2 Q_m} \quad (6)$$

In the same way, the mechanical power per area required to initiate adhesive fractures can be computed and is expressed by:

$$P_{mech} = \frac{U_{mod} \cdot \omega \tau_{adm}^2}{\tau_{mod}^2 Q_m} \quad (7)$$

The first terms of these expressions (6),(7) can be used as criteria :

$$C_{shear} = \frac{U_{mod} \omega}{\tau_{mod}^2} \quad \text{and} \quad C_{tensile} = \frac{U_{mod} \omega}{\sigma_{mod}^2} \quad (8)$$

These criteria are independent of the amplitude of the vibration. Having a high magnitude criterion shows that the structure is able to produce high level of stress in the ice without requiring a lot of power. Therefore, the lower the criterion value the lower the power consumption. The criteria are also independent from some non-geometric variables, which permits comparing results in a very quick way. Indeed, for example, consider that the required power per area according to the ice shear strength is under study. This is a usual test case since this strength is highly dependent on substrate roughness, temperature, ice grain size, flow speed... [13], [14], and this parameter is of major importance for researchers studying ice-phobic coatings. The impact over power requirement of different ice-phobic coatings can be investigated by performing a single Finite Element analysis to compute the criterion  $C_{shear}$ . Then, power is computed by multiplying this ratio by  $\frac{\sigma_{adm}^2}{Q_m}$  according to mechanical properties inputs.

#### IV. Criteria for Studying Fracture initiation

Two different fracture initiation mechanisms are observed in papers reporting experimental results on de-icing by mechanical effect [7], [15]. It appears that the fracture can be initiated on the top of the ice layer (cohesive initiation due to tensile stress) or directly at the ice/substrate interface (adhesive initiation due to shear stress). These two initiation mechanisms are here identified as tensile stress dominant mechanism and shear stress dominant mechanism.

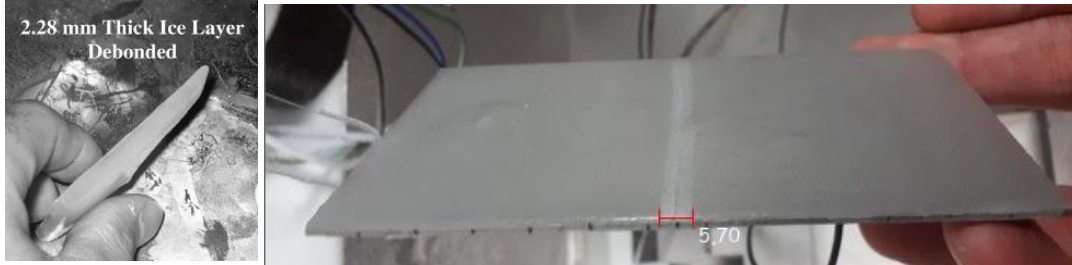


**Figure 3 Shear stress delamination (a) [7] and tensile stress cohesive fracture (b)**

With the approach mentioned in section II, two criteria are defined, computed in this article for flexural modes:

$$C_{tensile} = \frac{U_{mod.\omega}}{\sigma_{mod}^2} \quad \text{and} \quad C_{shear} = \frac{U_{mod.\omega}}{\tau_{mod}^2} \quad (9)$$

These criteria enable the comparison of the mechanical power level required for flexural modes to initiate cohesive fracture ( $C_{tensile}$ , tensile stress dominant mechanism) and adhesive fracture ( $C_{shear}$ , shear stress dominant mechanism) using relations (7),(9).

Computations are made using the FEM software ANSYS with the Mechanical module. A two-dimensional model of a half beam, compound of an ice layer and a substrate layer, is realized in order to facilitate and speed up the computations. The ice layer is divided in three surfaces (Figure 4), which are used to study the fracture propagation in the next section. The dimensions of these surfaces are variable to study different cases of fracture propagation. On one end of the beam, a symmetric condition is set and on the other end, an anti-symmetric condition is set. Triangle elements are used to mesh the two-dimensional geometry and the plain strain hypothesis is used for computations. The meshing size is set to a maximum value corresponding to a tenth of the smaller dimension in order to ensure a sufficient number of elements in each direction.

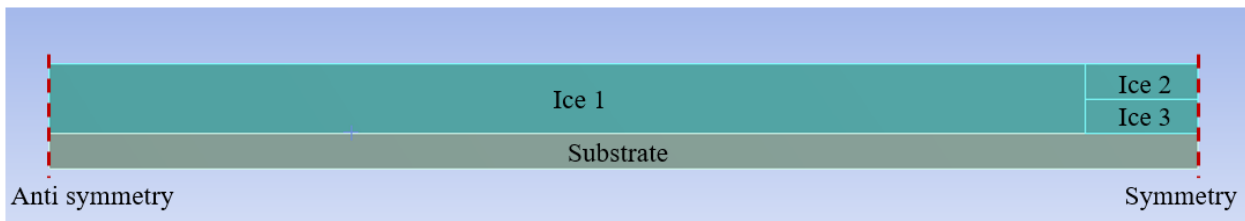


**Figure 4 - Finite element model geometry**

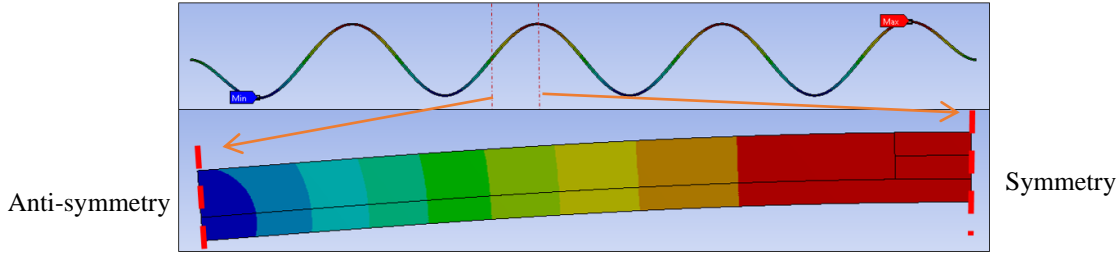


**Figure 5 Comparison between "infinite" beam deformation and model deformation**

The modal analysis is used to obtain the deformation profile of the beam. The first flexural mode of the model where the symmetric side is on the anti-node and where the anti-symmetric side is on the node is studied. Our simplified approach is based in the assumption of a beam of finite dimensions with symmetrical conditions at its two ends makes it possible to simulate the behavior of a beam of infinite length for different frequencies. As the length of the model is being shortened, the behavior of the first vibration mode of the model represents the behavior of the infinite beam at higher frequency. Therefore, this model allows studying the whole frequency range by modifying its length. There are limits to this model. It is only valid in the case of a beam with several nodes and anti-nodes and for areas with nodes and anti-nodes far from the ends of the beam. For high frequency solutions, the model well simulates the behavior of most nodes / anti-nodes. In the case of low frequency beams (one or two nodes), the model is not representative and a specific study is required. Nevertheless, the proposed model allows establishing trend curves useful for design.

In order to compute fracture initiation criteria, the stresses in the structure must be computed. The first principal stress (tensile stress intensity) in the ice is computed and referred as  $\sigma$  in order to study cohesive fracture initiation. For the adhesive fracture initiation, the shear stress at the ice/substrate interface is computed and referred as  $\tau$  (on the ice side) as it was identified as the weakest adhesive de-bonding condition [16]. Two areas with different kind of fracture initiations are identified. For the cohesive initiation, the maximum tensile stress is located on the ice surface at the anti-node location (symmetric condition). For the adhesive initiation, the maximum shear stress is located on the node (anti-symmetric condition).

The computation of  $C_{tensile}$  and  $C_{shear}$  criteria for flexural modes are plotted in Figure 6 for the following geometry: 1 mm-thick titanium substrate and 2 mm-thick ice layers.

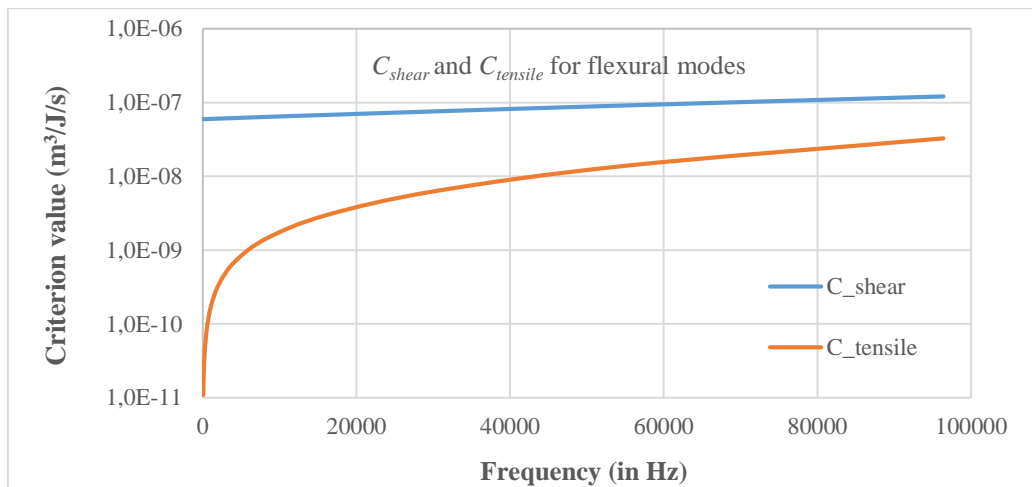


**Figure 6 Criteria  $C_{tensile}$  and  $C_{shear}$  according to the frequency**

Figure 6 shows that for flexural modes, less power is required to create (at location previously defined) a given amount of tensile stress than to create the same amount of shear stress. However, the amount of stress required to initiate fracture is not the same for both mechanisms since the mechanical strength of the material is not the same for tensile and shear loads.

## V. Criteria for Studying Fracture propagation

### A. Proposed methodology for the criteria computation

In order to perform efficient de-icing, the fracture needs to propagate after being initiated. To study the propagation of fractures, the classical Griffith energy balance approach is used. In the energy balance approach, it is assumed that a certain amount of energy is absorbed by the structure during the formation of a fracture. When the fracture propagates, a certain amount of stored elastic energy is released which enables to define the energy release rate  $G$  with  $U$  the strain energy in the structure,  $l_f$  the length and  $b$  the depth of fracture:

$$G = -\frac{1}{b} \left( \frac{dU}{dl_f} \right) \quad (10)$$

The fracture grows in an unstable way if the energy release rate  $G$  is equal to or greater than the critical energy release rate  $G_c$  whereas it does not grow if the energy release rate  $G$  is lower than the critical energy release rate  $G_c$  of the material [17]. However, increasing the energy going into the system (load, displacement...) will rise the strain energy level and thus the  $G$ . The fracture will grow in a stable way as the energy release rate  $G$  reaches the critical energy release rate  $G_c$  of the material. Three cases are therefore considerable. If  $G$  is lower than  $G_c$  the fracture does not propagate. If  $G$  is equal to  $G_c$  the fracture propagates in a stable way. And if  $G$  is greater than  $G_c$  : the fracture propagates in an unstable way. When  $G$  is lower than  $G_c$ , increasing the strain energy in the structure will increase the  $G$  leading to a stable crack propagation, as the energy release rate reaches the critical value. Figure 7 illustrates these two modes of crack propagation for which specific analysis criteria will be defined.

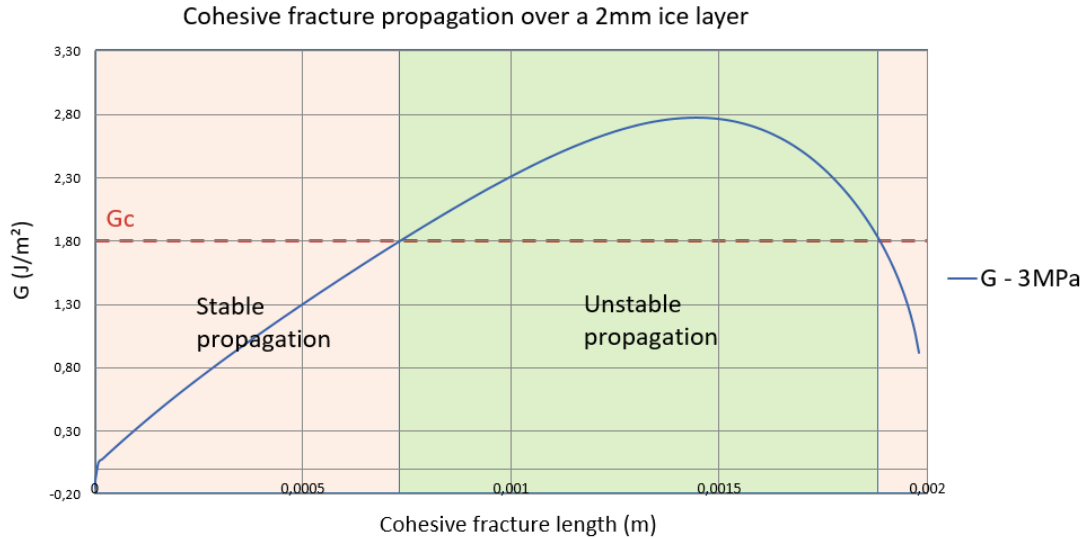


**Figure 7 Energy release rate  $G$  of cohesive fracture propagation for a given amplitude (Flexural mode)**

The computations of the energy release rate and criteria for fracture propagation are done assuming the crack propagation path according to two mechanisms defined in [15]. “Mechanism 1” starts with the initiation of cohesive fractures by tensile stress at the top surface of the ice layer. The cohesive fracture propagates within the ice and eventually, propagates at the ice/substrate interface in an adhesive way starting from the base of the cohesive fractures previously created. “Mechanism 2” is defined by initiation and propagation of adhesive fractures at the ice/substrate interface, by shear stress.

To compute the energy release rate, the finite element model defined in 0 is used. For fracture mechanism 1, the cohesive fracture is simulated by removing the symmetric condition on the right edge of the Ice 2 surface (Figure 8). Hence, it is possible to modify the crack length by modifying the thickness of Ice 2 surface. It was ensured that modifying the size of each face for a given configuration had no impact on the computation results.

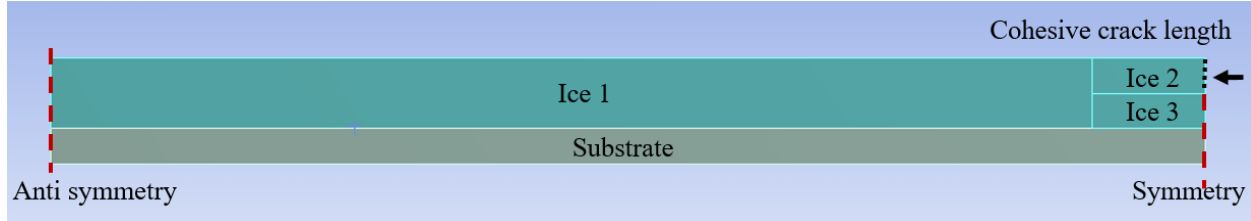


**Figure 8 Finite element model for cohesive crack propagation**

For the adhesive part of mechanism 1, the fracture propagation could have been simulated by removing the contact between Ice 3 and the substrate. However, for extended adhesive fractures, the modal analysis is disturbed and the first mode becomes a mode where only the detached ice block is vibrating going down to extremely low frequencies. To avoid this issue an assumption was made on the strain energy inside the de-bonded ice bloc. It is assumed and verified that, when the contact between Ice 3 and the substrate is removed, the elastic strain energy inside the ice block is close to zero. This hypothesis allows computing the  $G$  value regardless of the strain energy of Ice 2 and Ice 3. Hence, it is possible to remove the ice blocks from computation. Therefore, the adhesive propagation of the fracture is made by removing Ice 2 and Ice 3 and shortening the length of Ice 1 (Figure 9).

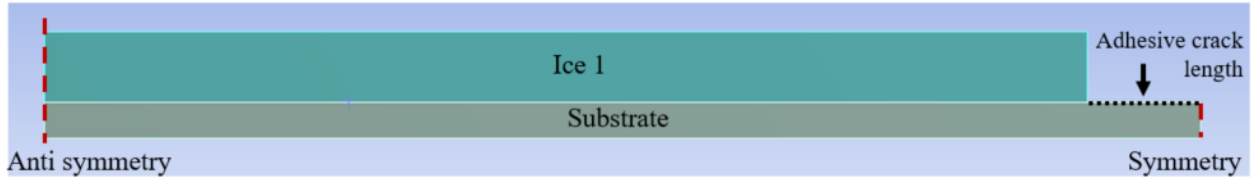


**Figure 9 Finite element model for adhesive crack propagation with mechanism 1**

Fracture mechanism 2 begins with the initiation of an adhesive fracture on the node side at the ice/substrate interface. In this case, the fracture propagation is simulated by removing the contact between Ice 1 and the substrate and progressively increasing the Ice1 length (Figure 10).

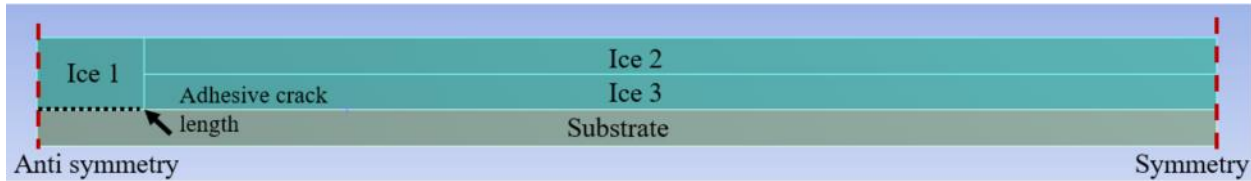


**Figure 10 Finite element model for adhesive crack propagation with mechanism 2**

Stable crack propagation occurs when the energy release rate  $G$  of the fracture propagation reaches the critical energy release rate  $G_c$  (previously being under the critical value). In our case, after the crack initiation, the overtaking of the critical release rate value can be done by increasing the vibratory amplitude. Nevertheless, if the actuation power supply is switched off, the crack will stop its growth, hence its stable definition. In stable crack propagation configuration, crack growth is controlled by monitoring the applied load, in our case, the amplitude of vibration and the subsequent elastic strain energy. The computed value of the modal energy release rate depends on the modal strain energy density:

$$G \propto U \propto x^2 \quad (11)$$

In the same way, unstable crack propagation occurs if the energy release rate  $G$  of the fracture propagation is equal or greater than the critical energy release rate  $G_c$  (previously being over the critical value). Therefore, the criteria required

to study and quantify crack propagation phenomenon and power requirements are related to energy release rate and are defined in a similar way as to the ones used to study crack initiation, i.e.:

$$C_{coh_{x\%}} = \frac{U_{mod_{x\%}} \cdot \omega}{G_{coh_{x\%}}} \quad \text{for cohesive fracture propagation} \quad (12)$$

$$C_{adh_{x\%}} = \frac{U_{mod_{x\%}} \cdot \omega}{G_{adh_{x\%}}} \quad \text{for adhesive fracture propagation} \quad (13)$$

These criteria based on the modal energy release rate allow evaluating the power required to propagate the fractures on a percentage ( $x\%$ ) of the total fracture length according to the type of modes and the fracture mechanisms.  $G_{adh_{x\%}}$  is the modal energy release rate for an adhesive fracture of length  $x\%$  and  $G_{coh_{x\%}}$  for a cohesive fracture of length  $x\%$ . These criteria allow comparing different modes, regardless of the amplitude of the deformation. In the same way as in section II, the criterion can be used to compute power requirement using mechanical properties of the material and the structure.

$$P_{mech} = \frac{U_{mod} \omega}{G_{coh_{x\%}}} \frac{G_c}{Q_m} = C_{coh_{x\%}} \frac{G_c}{Q_m} \quad (14)$$

With  $G_c$  the critical energy release rate in J/m<sup>2</sup> and  $Q_m$  the resonant quality factor of the mode under study. Criteria  $C_{adh_{x\%}}$  and  $C_{coh_{x\%}}$  are expressed in m<sup>3</sup>/J/s.

## B. Computation of criteria for mechanism 1

First, the  $C_{coh_{x\%}}$  criterion is computed to analyze the impact of the frequency on the power level for the propagation of cohesive fractures (Figure 11) through the ice thickness. The descending shape of the curves shows that for early stages of the propagation (fracture length of a few %), the propagation of the crack is highly unstable. This means that if the power required to begin the propagation (according to the crack length after initiation) is supplied, the propagation will be instantaneous up to the interface. Figure 11 also highlights the fact that for lower frequencies (lower rank modes) the cohesive propagation tends to require less power.

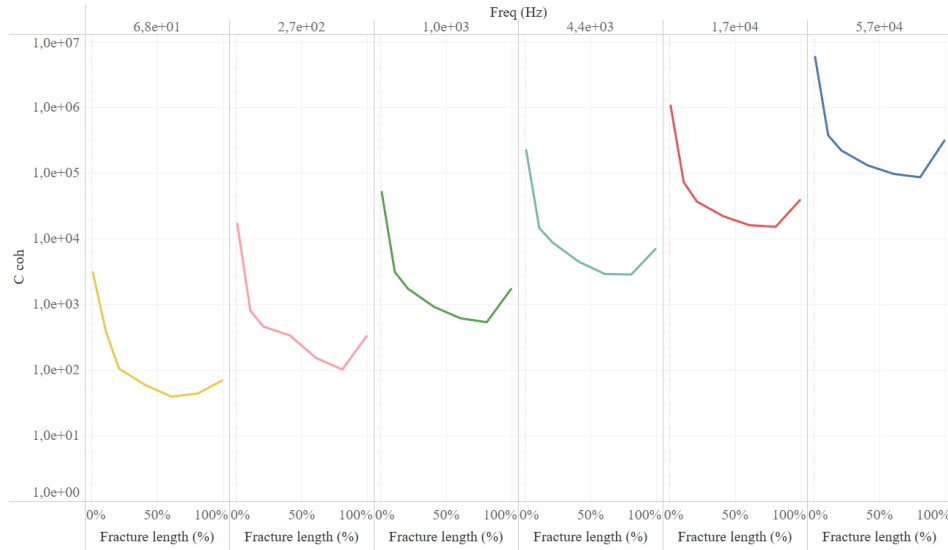


**Figure 11 -  $C_{coh,x\%}$  for cohesive fracture propagation (mechanism 1) for various frequencies**

Upon reaching the interface, the cohesive fracture stops and the adhesive fracture begins along the ice/substrate interface. The  $C_{adh,x\%}$  criterion is studied to compare the impact of the frequency on the adhesive propagation power level. Figure 12 is established assuming that the propagation of the adhesive fracture starts once the cohesive fracture completed. The figure highlights the fact that the lower the frequency (low rank modes) the lower the power requirements. Moreover, the increasing shape of the curves shows that, while the fracture extends, the power required to pursue the propagation increases. The propagation of the adhesive fracture with this mechanism is therefore stable.

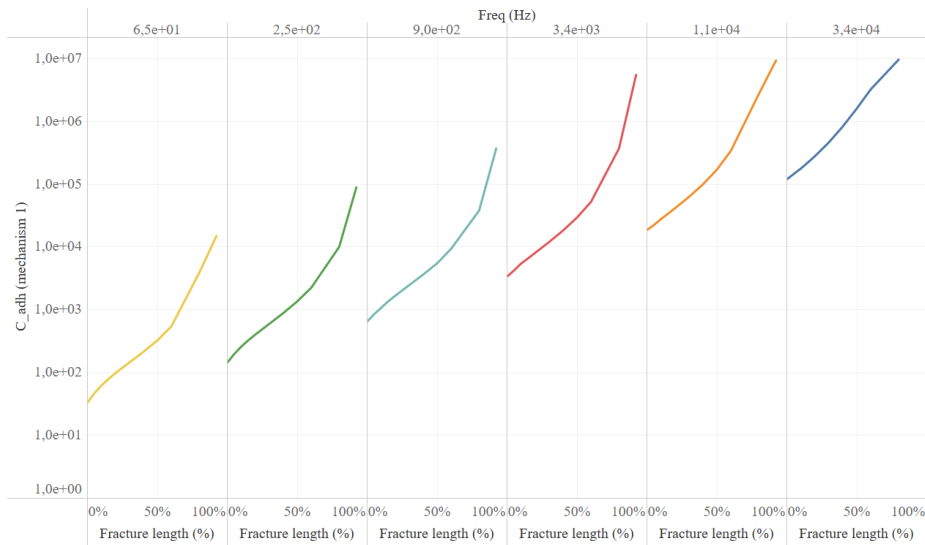


**Figure 12  $C_{adh,x\%}$  for adhesive fracture propagation (mechanism 1) for various frequencies**

### C. Computation of criteria for mechanism 2

The second mechanism is the shear mechanism. There is no cohesive fracture initiation. After adhesive initiation, the fracture propagates at the ice/substrate interface from the node (Figure 10). Figure 13 gives the propagation criterion for the adhesive fracture in mechanism 2 and the descending behavior of the curves shows that this mechanism is an unstable mechanism. As for the cohesive propagation of the mechanism 1, if the power required to begin the propagation is reached, the crack will propagate instantaneously to the anti-node. Exciting low frequencies (low rank modes) appears to be more beneficial for the propagation of the fracture.

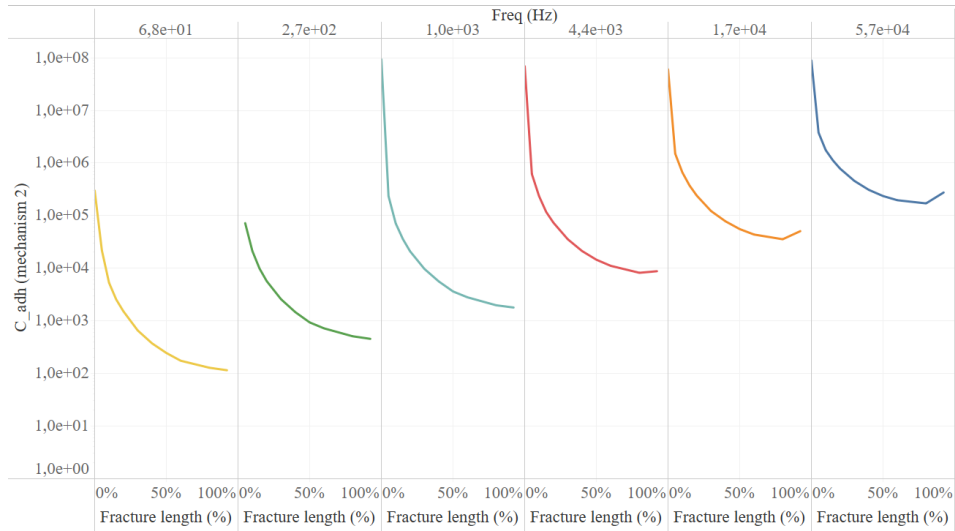


**Figure 13  $C_{adh,x\%}$  for adhesive fracture propagation (mechanism 2) for various frequencies**

The use of the criteria also enables fast comparisons between different mechanisms. For example, it is possible to compare the  $C_{adh,x\%}$  criterion of mechanism 1 to the  $C_{adh,x\%}$  criterion of mechanism 2 at their observable frequencies (Figure 14). For mechanism 1, 1kHz is used to comply with model limits and ensure a significant number of nodes between beam tips. For mechanism 2, the frequency of 50 kHz is chosen as it is the lowest frequency for which the mechanism can occur (explained in next section).

Without having to compute the real power requirement, it is already possible to conclude on the efficiency of a mechanism. To begin the unstable propagation, mechanism 2 will require 200 times more power than mechanism 1 to propagate fracture up to 90% of the interface ( $10^8$  vs  $5.10^5$ ). A compromise is therefore required between high power and full protection and lower power and partial protection.

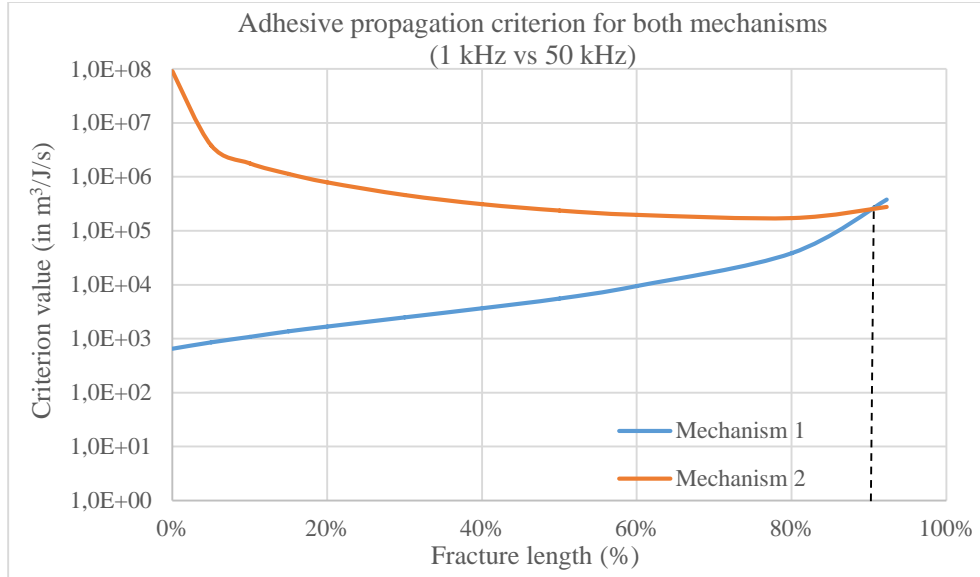


**Figure 14**  $C_{adh,x\%}$  for both mechanism 1 and mechanism 2 at their observable frequencies

Table 1 summarizes the conclusions made from the study of the criteria introduced previously.

**Table 1 : Propagation mechanisms summary**

<b>Cohesive propagation</b>	<b>Adhesive propagation (mechanism 1)</b>	<b>Adhesive propagation (mechanism 2)</b>
Unstable propagation	Stable propagation	Unstable propagation
Lower power requirements with low mode rank	Lower power requirements with lower mode rank	Lower power requirements with lower mode rank

## VI. Numerical Results and Configuration Selection

In this section, an analysis based on the criteria will be proposed for the plate under study to analyze advantages and drawbacks of each type of mode. Power values for initiation and propagation will be computed using criteria defined previously to highlight the most power-efficient de-icing strategies.

### A. Numerical Results for Fracture Initiation

Using mechanical properties of ice defined in Table 2 and a quality factor  $Q_m$  of 50 (which is a fair value for flexural modes according to various experimental measures [8]), the power required to initiate cohesive and adhesive fracture is computed using relation (7) and plotted in Figure 15 for both mechanisms.

**Table 2 : Ice strength [18], [19]**

Mechanical properties in ice and at the ice/structure interface	
Ice Cohesive strength	[0.6-3] MPa
Adhesive shear strength (ice/structure)	[0.2-1] MPa

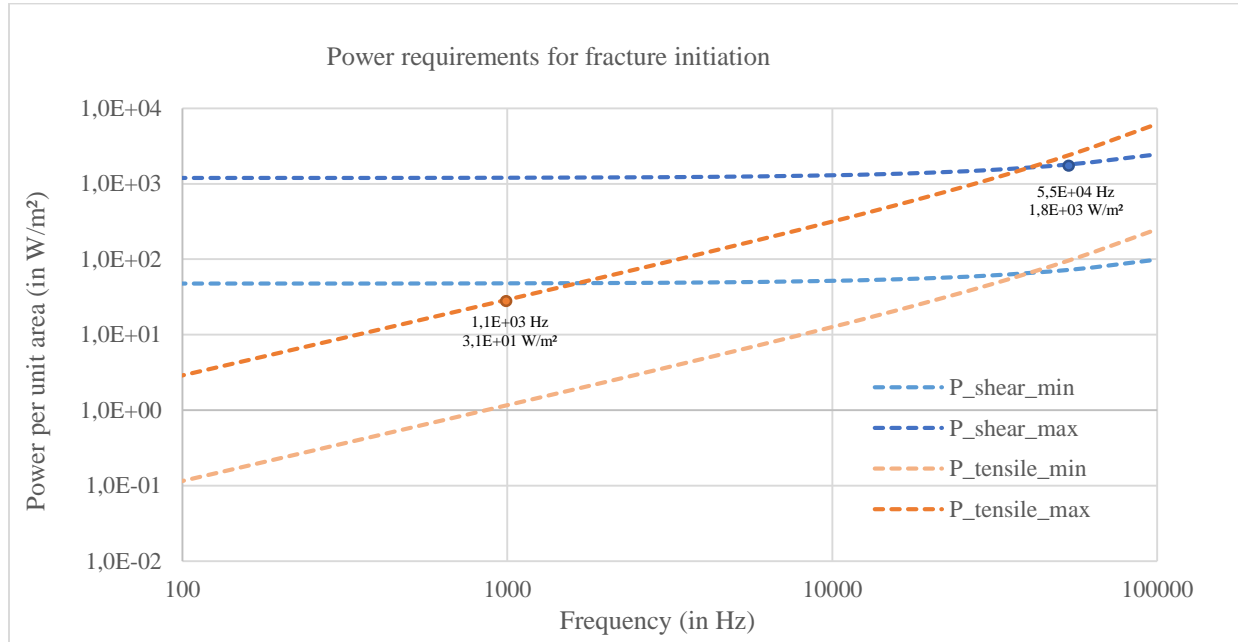


**Figure 15 Power requirement for fracture initiation by tensile or shear stress**

Figure 15 shows that, for standard adhesive shear strengths without coating and for low frequencies (low rank modes), power requirements for initiation by tensile stress are much lower than power requirements for initiation by shear stress. Therefore, for low rank modes, initiation of adhesive fracture is not observable.

On the other hand, for high frequencies (high rank modes), the power requirement for initiation by tensile stress can exceed the power requirement for initiation by shear stress and thus initiation of adhesive fracture at the interface is more likely to occur. Figure 15 also highlights the fact that the uncertainty on the mechanical strength of the ice or interface makes it difficult to estimate the power requirements with accuracy. Nevertheless, it is still possible to assess maximum values using top strength values. For example, the power required for initiating a cohesive fracture using a flexural mode around 1 kHz is assumed to be around 30 W/m<sup>2</sup> for ice with high cohesive strength. In the same way,

the power required for initiating an adhesive fracture at the ice/substrate interface with a flexural mode at 50 kHz will be 1.8 kW/m<sup>2</sup>.

### B. Numerical Results for Fracture Propagation

Using the mechanical properties of ice defined in Table 3, a quality factor  $Q_m$  of 50 and relation (14), the power required to propagate the fracture to the  $x\%$  length can be computed.

**Table 3 Ice energy release rate [20]**

Mechanical properties in ice and at the ice/structure interface	
Critical strain energy release rate, $G_c$ (ice or ice/structure)	[0.5-1] J/m <sup>2</sup>

#### *Mechanism 1*

Figure 16 shows that, in order to reduce power requirements for cohesive fracture propagation, low frequency modes are more efficient when it comes to propagate cohesive fractures on the anti-node location. Two power curves are drawn, for the two extremes values of  $G_c$  found in the literature (Table 3). The light curve represents the power for the lowest  $G_c$  value whereas the darkest one represents the power for the highest one. In order to achieve the full propagation of the cohesive crack (2 mm ice thickness) for a 1 kHz mode frequency, the required power is 1.0 kW/m<sup>2</sup>. It is important to understand that since the propagation is unstable, the power requirement value is not the power value of the  $x\%$  length but the power value for fracture initiation.

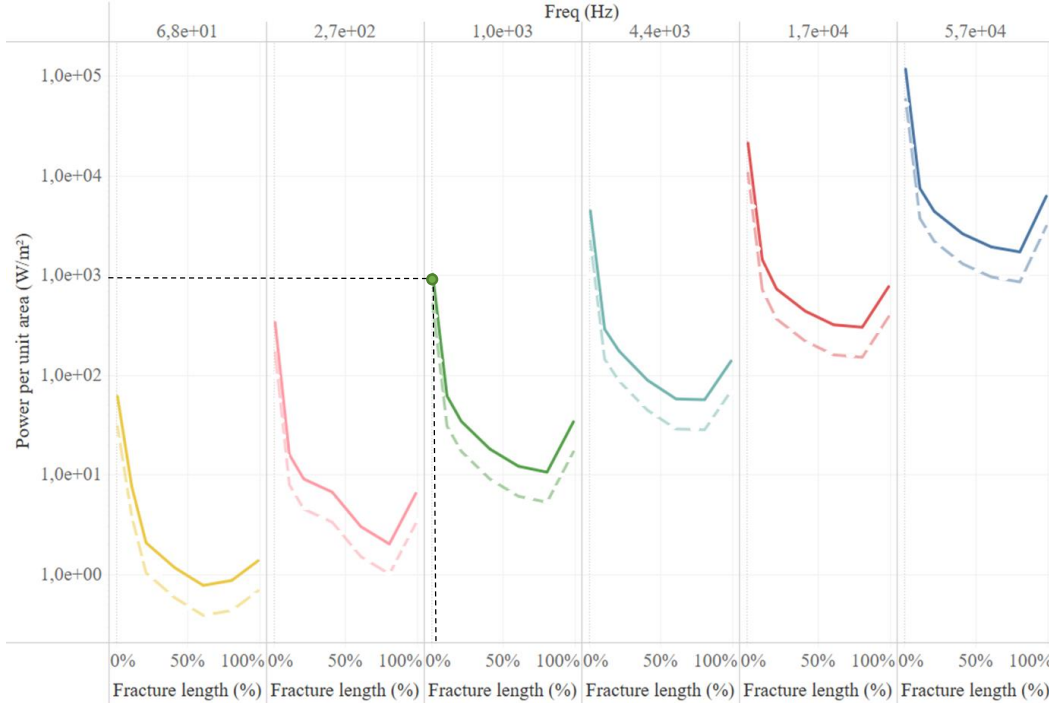


**Figure 16 Power requirements for cohesive fracture propagation according to the frequency**

In the same way, it is possible to compute the power required for propagating adhesive fractures in mechanism 1. Figure 17 shows, as it was expected from the plot of the  $C_{adh}$  criterion, that the power requirements are lower for low

frequencies (low rank modes). The light curves are the power curves for the lowest value of  $G_c$  (0.5 J/m<sup>2</sup>) whereas the darkest curves are the power curves for the highest value of  $G_c$  (1.0 J/m<sup>2</sup>). From these curves, the power requirements to propagate the adhesive fracture to a given length can be estimated. For example, at the frequency of 900 Hz, the power required to propagate adhesive fracture over 50% is around 100 W/m<sup>2</sup> and the power has to be increased to 5.5 kW/m<sup>2</sup> to propagate adhesive fracture over 90% of the interface length.

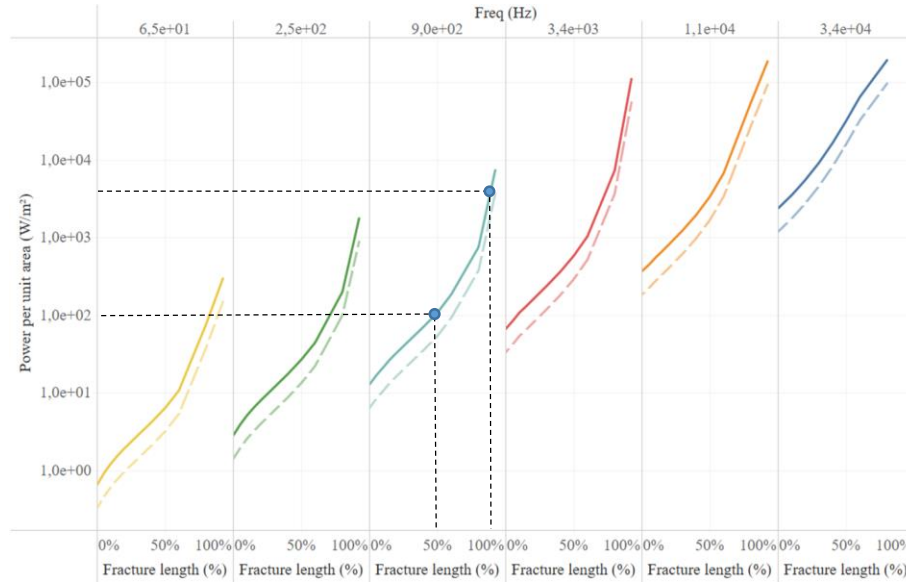


**Figure 17 Power requirements for adhesive fracture propagation (mechanism 1) according to the frequency**

### *Mechanism 2*

Figure 18 shows that as, for mechanism 1, the power requirements are lower for low frequencies (low rank modes). However, as shown in Figure 15, mechanism 2 can only be initiated with high frequencies, since mechanism 1 as lower power requirements in such frequency range. In our case, the minimum frequency is around 50 kHz. From Figure 18 curves, we can estimate the power requirements to propagate the adhesive fracture to a given length. Due to its unstable behavior, the power required is the minimal power to begin the propagation. For example, at the frequency of 57 kHz, the power required to begin the propagation and therefore extend it instantaneously to 100% is around 1.0 MW/m<sup>2</sup>. However, if a crack covering 25% of the interface length already exists, the power required to propagate the fracture to 100% would be under 10 kW/m<sup>2</sup>.

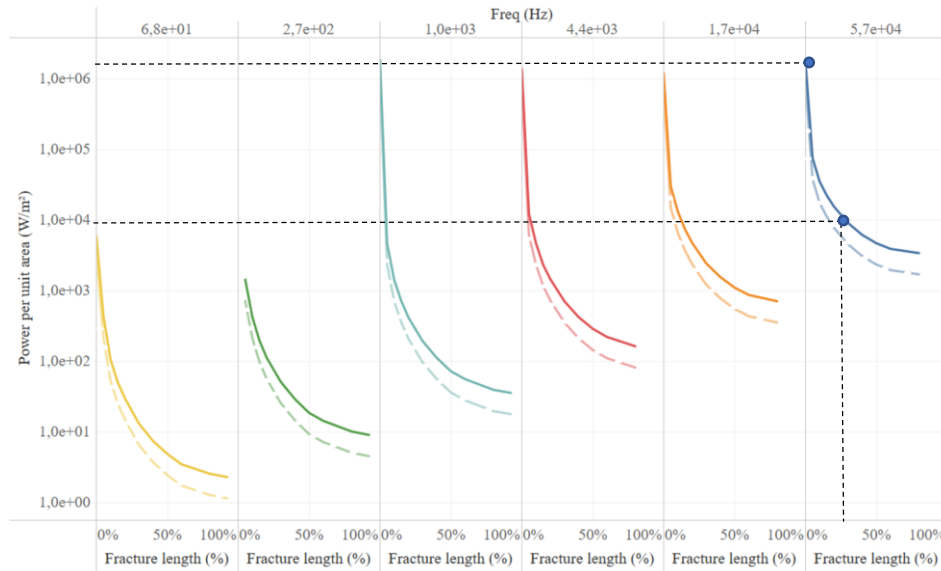


**Figure 18 Power requirements for adhesive fracture propagation (mechanism 2) according to the frequency**

### C. Selection of flexural modes-based configurations for electromechanical deicing purposes.

Mechanism 1 shows fairly low power requirements when it comes to initiate the fracture, especially for low rank modes. Due of its unstable behavior (Figure 11) the creation of the cohesive fracture over the entire ice thickness appears to be instantaneous after initiation and does not require a lot of power, especially for low rank modes. For the propagation of the adhesive fracture, due to the stable behavior shown in Figure 12, the power has to be increased to extend the propagation length. The power requirement to protect  $x\%$  of the substrate can be computed thanks to equation (14).

The initiation of the adhesive fracture in mechanism 2 is only possible for high frequencies. Computations show that mechanism 2 would offer an instantaneous and complete protection thanks to the unstable behavior of the propagation. Nevertheless, the power required to start the propagation is relatively high and, consequently, the lowest frequency for which mechanism 2 can occur has to be selected.

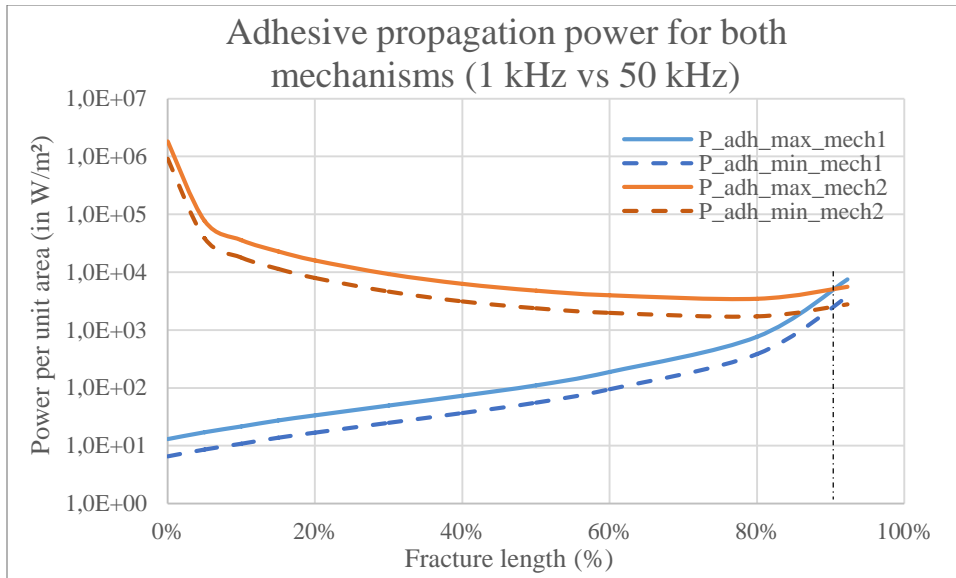


**Figure 19 Power requirement for adhesive fracture propagation by tensile stress (1 kHz) or shear stress (50 kHz)**

Using criteria shown in Figure 17 and Figure 18 and mechanical properties from Table 3, power requirements for adhesive fracture propagation by shear and tensile stress are computed at the most probable frequency for each mechanism. Figure 19 shows that it would cost around 5.5 kW/m<sup>2</sup> to protect 90 % of the area using mechanism 1, and that it would cost around 1 MW/m<sup>2</sup> to protect the entire surface using mechanism 2 (the 200 ratio observed in Figure 14 is still observable here). However, for mechanism 2, the high consumption part of the fracture propagation is the early stage of the fracture. If an adhesive pre-crack of 10% length is created using another device, the required power to propagate the fracture over the last 90% (100% of effective protection) should be around 35 kW/m<sup>2</sup>. Comparing solutions, even if the protection is not full, the mechanism 1 offers over 90% protection for power requirements way under mechanism 2 requirements.

## VII. Experimental verification

### A. Experimental devices

Experimental campaign is realized to confront computations and models to experimental results. The objective is to check for both mechanisms if assumptions made from finite element analysis are correct and if the mechanisms identified are observable. The experiment should confirm the initiation on the anti-node for low frequency excitation and the propagation of the adhesive fracture along the interface. For high frequency excitation, no cohesive fracture should be observed and adhesive delamination should occur. The power computations should also enable estimating whether or not the observation of such mechanisms is possible for a given power supply.

The substrate consists in a titanium plate of 130 mm length, 50 mm width and 1mm thick. Ice is accreted on the surface of the substrate by spraying fine particles at low temperature (close to 0°C) in a freezing environment (-20°C). The spraying of the water is only done when plate temperature has reached the low environment temperature. According to the thickness desired, the quantity of sprayed water is adjusted to reach the right thickness.

The actuation of the plate is made using piezoelectric ceramics, which are bonded to the non-iced face of the titanium plate. To reduce heating effects (especially for high frequency tests), hard piezoelectric ceramics were used (PIC 181 from PI). The test sample is tested in free boundary conditions thanks to the use of nylon strings holding it in the freezing environment. It is assumed that the stiffnesses of the strings are negligible so the system can be considered in free conditions.

First, 3D models of the sample were realized (with a 3 mm-thick ice layer and without ceramics) to compute fracture initiation power requirements. A modal analysis is run to compute every single existing mode in the range 0 to 100 kHz. Two modes were selected to study both mechanism 1 and mechanism 2. To study mechanism 1, the first flexural mode was selected to reduce power requirements as much as possible. To study mechanism 2, a mode with power requirements for initiation by shear stress lower than those for initiation by tensile stress has to be selected. Using the power computation from Figure 20, it appears that to initiate a fracture at the interface, the flexural mode has to be excited at a frequency above 50 kHz. In order to reduce the power consumption as much as possible, the first flexural mode existing over 50 kHz was selected.

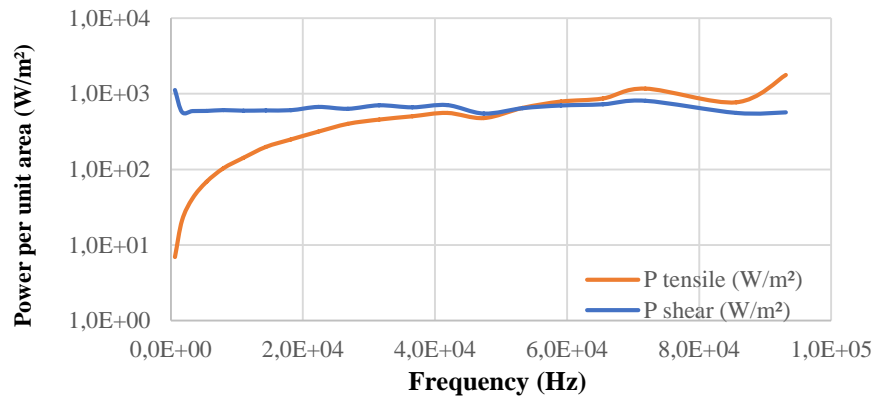
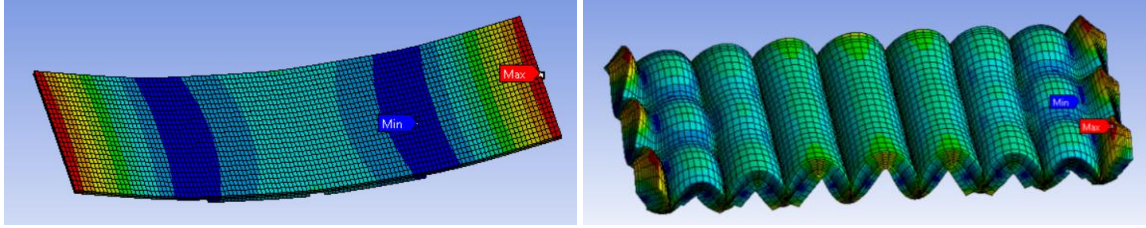
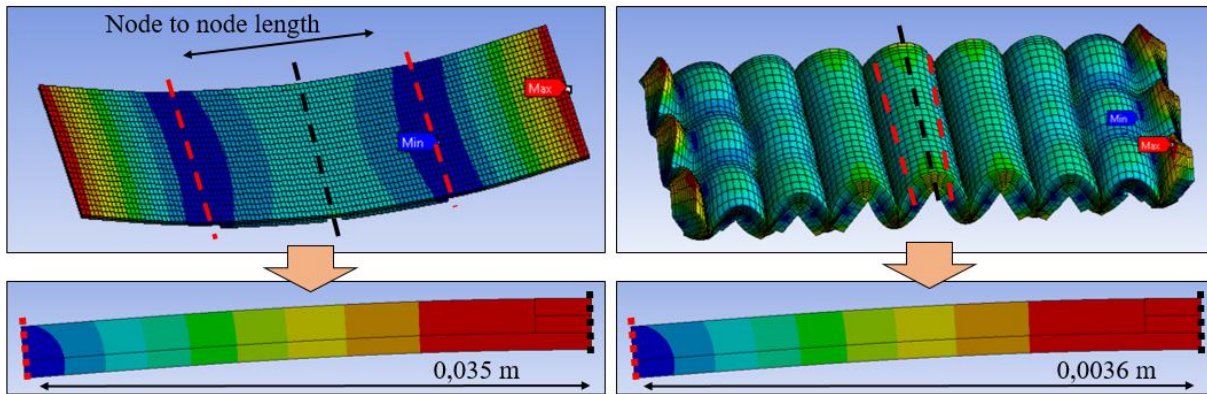


Figure 20 Power requirements for fracture initiation by tensile or shear stress



**Figure 21** Finite element modal shape of the two selected modes: 923 Hz and 57 kHz

Using modal deformation from Figure 21, 2D models are realized to fit with the experimental samples. For the low frequency sample, the node to node length is measured and the half beam model is created with matching lengths (Figure 22). A 2D model is also made to match with the high frequency sample using the same method.



**Figure 22** 2D model creation from 3D modal deformation computations

Then the power requirements for propagating adhesive fracture propagation are estimated with the 2D finite element computations for both samples (Figure 23). The objective is to compare these powers to the lab power supply which has a maximum power of 300W and a voltage range of [-200, +200] V. According to this 2D analysis, mechanism 1 requires 60 W and should be observable and the power supply should allow delamination up to 90% of the node to node surface corresponding to 48% of the length of the plate. However, mechanism 2 power requirements reach 5.0 kW and exceed the power supply limits, making the adhesive fracture propagation unobservable. Nevertheless, the adhesive fracture initiation from shear stress should occur (10 W).

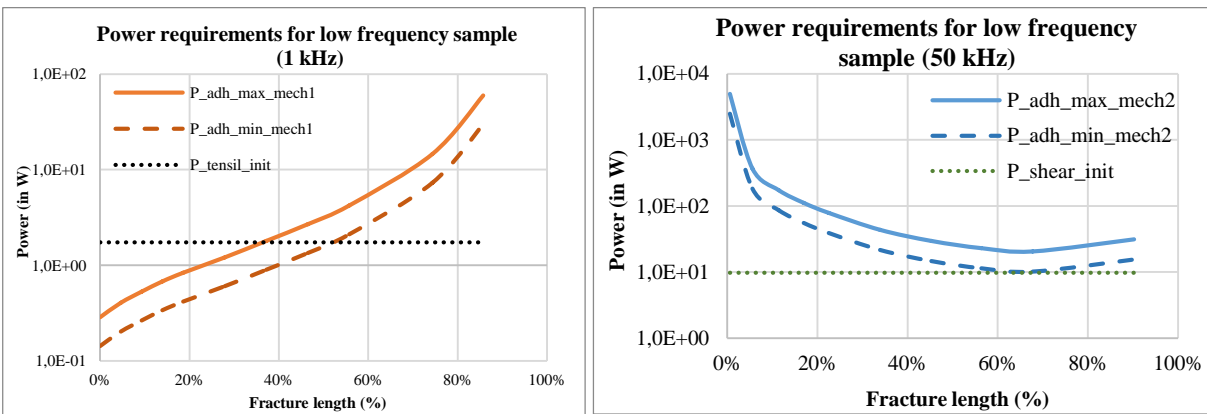


**Figure 23** Power requirements for adhesive fracture propagation and mechanism initiation

To be able to excite properly both modes (Figure 21), two samples are realized with piezoelectric ceramics for actuation and sensing. The actuators set up is adapted on both samples to optimize the coupling with the structure. Finally, a last modal analysis is run to ensure that the positioning of actuators and sensors does not alter too much the resonance of the structure. Samples are then manufactured. The titanium plates are polished to ensure a similar surface condition between both samples. PIC 181 ceramics are cut to desired sizes and bonded to the plates using conductor epoxy resin. The total surface of actuators is arranged to remain the same on both samples (Figure 24). Ceramics are placed in a symmetrical way in order to have a good image of the actuators coupling while monitoring with the sensor (actuator and sensor configuration). This kind of set up also allows using both ceramics (or sets of ceramics) as actuators if needed (double actuator configuration).

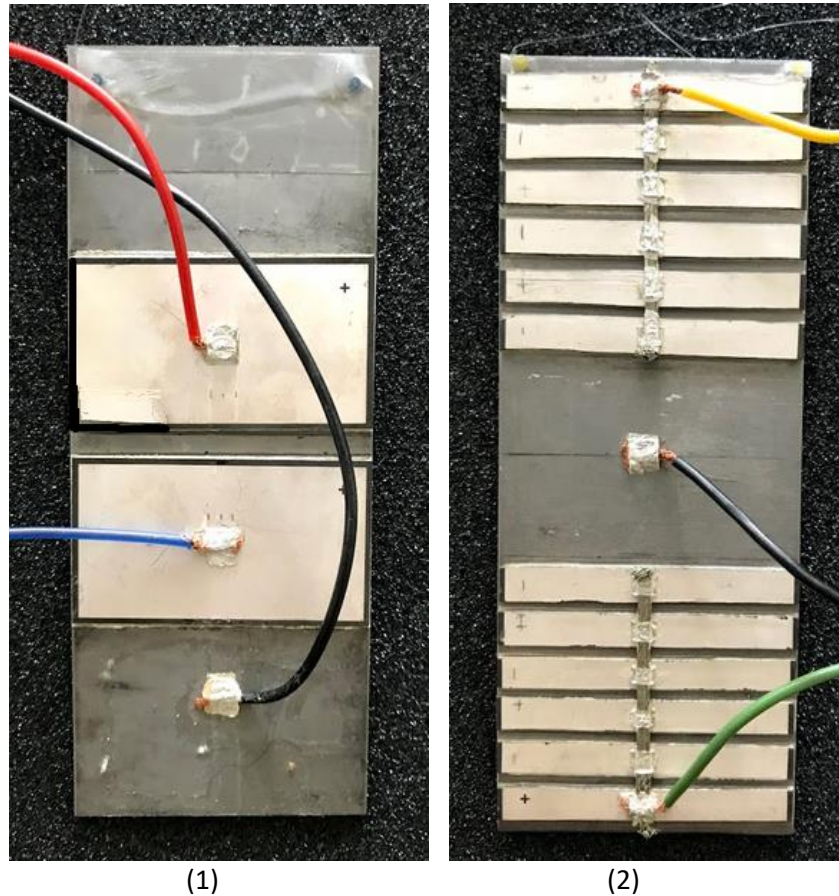


**Figure 24 Test samples: (1) for studying mechanism 1 – (2) for studying mechanism 2**

### **B. Low frequency mode – mechanism 1**

First, mechanism 1 is tested with the objective to observe the fracture mechanism at work. Finite element computation is made for a homogenous ice layer of 3mm (Figure 25). The first mode frequency is computed to be 923 Hz. Using the methods described in previous sections, the power to initiate the cohesive fracture using tensile stress is estimated to have a magnitude of 0.05 W for this sample. The power to initiate an adhesive fracture at the interface using shear stress is estimated to have a magnitude of 0.9 W.

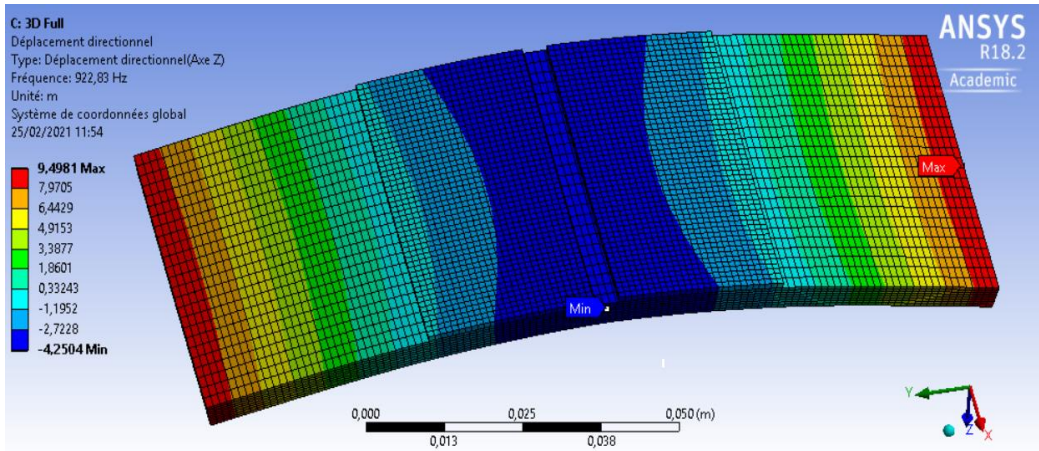


**Figure 25 Finite element simulation of first mode of bending with 3mm ice thickness**

First, tests at low voltage (15Vpk) (Figure 26) are performed to check the value of the first mode frequency (1089 Hz) and to measure the quality factor ( $Q_m = 110$ ). The initiation and propagation of the cohesive fracture are then studied. Several frequency sweeps are performed, increasing the voltage at each iteration until a crack is observed. A cohesive crack is observed during the 80 Vpk sweep (Figure 26) as the sensor voltage drops down a few times. A first small drop is observed on the spectrum, this concurs with the creation of small fractures shown in Figure 27. This figure shows that the fracture takes place on the anti-node, in the middle of the plate, as expected. As the sweep continues, the resonant frequency is caught up and the amplitude of the sensor signal rises for some frequencies. When the vibration amplitude gets high enough (getting closer to the resonant frequency), a full cohesive fracture is observed. A video of the experiment confirms that fracture is quasi-instantaneous and that the propagation of the fracture is unstable.

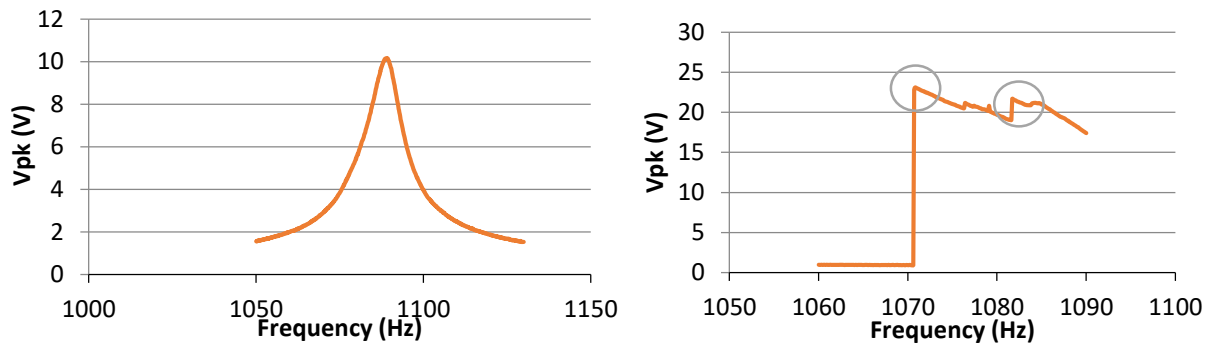


**Figure 26 Sensor voltage for 15 Vpk sweep with no crack versus 80 Vpk sweep showing multiple cracks in the width of the plate**

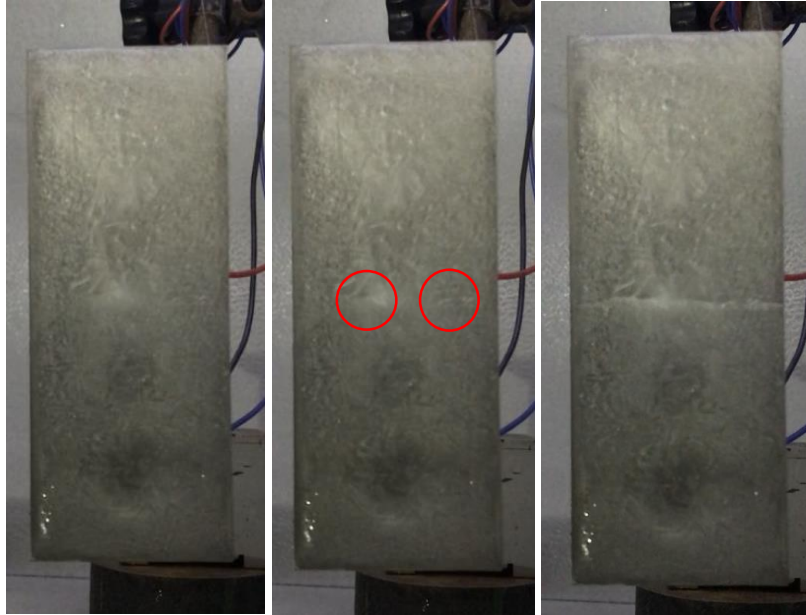


**Figure 27 Cohesive fracture states 80Vpk sweep. 1) No fracture. 2) Small fracture initiation. 3) Complete cohesive fracture.**

Once the cohesive fracture was observed, the propagation of the adhesive fracture was studied. The objective is to check if the adhesive fracture propagates from the edge of the cohesive fracture. A sweep is made to identify the new first mode frequency of the structure. The frequency shifted down to 800 Hz. To propagate the adhesive fracture, a descending frequency sweep is made to keep propagating the fracture while the frequency is shifting downward. Sweeps are performed, increasing gradually the input amplitude. At 150 Vpk, adhesive propagation is observed. The various peaks of Figure 28 correspond to the sequence of micro fractures propagating along the adhesive interface. For every step of the sweep, the power required to overcome  $G_c$  is supplied leading to a propagation of the crack over a small surface. This propagation induces a resonant frequency shift, which is caught up by the sweep, leading to a new exceeding of the required power and so on... Figure 29 shows pictures of the various stages of the propagation at 150 Vpk until the end of the propagation. To increase the delamination area, a second sweep is done with a higher voltage of 200 Vpk. As the power increases, the fracture extends. The same stable propagation mechanism is observed: Figure 30 shows that the delamination is greater than with 150Vpk but that the propagation stops. As the maximum voltage of the power supply is reached, to go further in the propagation, the sensor is converted into an actuator. Hence, no sensor output is available for the last sweep. The maximum amplitude configuration is launched, using the same sweep as before but with the two ceramics as actuators. The length of propagation obtained with such sweep is considered to be the maximum length obtainable with the laboratory set up. Figure 31 shows two fracture states for the sweep with two actuators at 200 Vpk (reaching the voltage limit of the power supply). On one side, the adhesive fracture propagates as planned, reaching a given length according to the power supplied. On the other side, a cohesive crack appears, preventing the adhesive fracture from going further. Finite element analysis of the damaged sample help explaining this unexpected cohesive crack apparition. As the criteria computation was done for “ceramic free” structure, sensibly different behavior can be expected from the real sample.

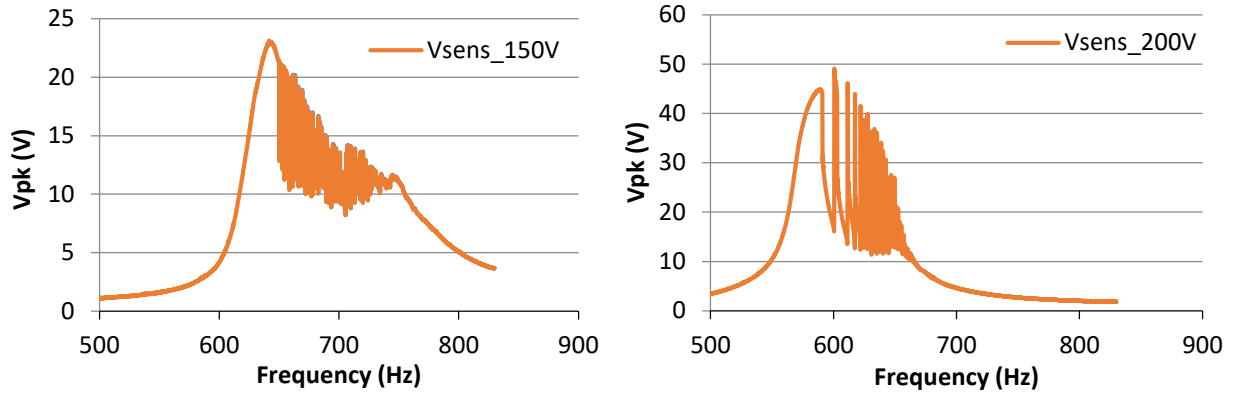


**Figure 28 Sensor voltage for 150 Vpk sweep and 200 Vpk sweep**

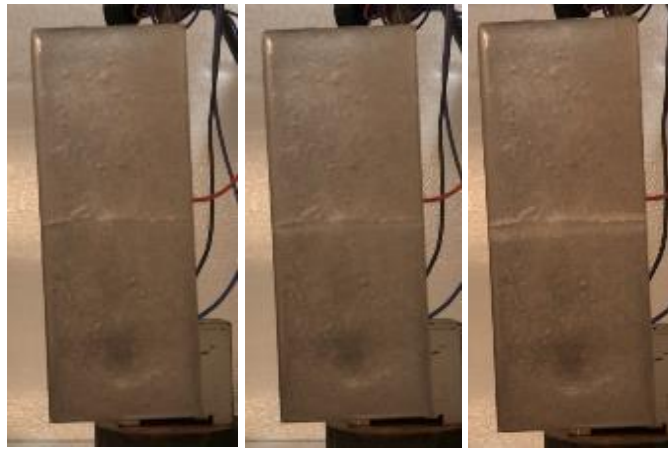


**Figure 29 Adhesive fracture states for 150Vpk sweep. 1) No fracture. 2) Beginning of the propagation. 3) Further propagation.**

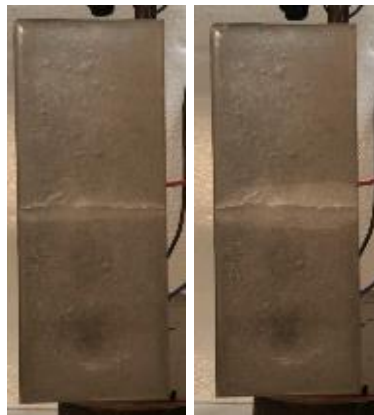


**Figure 30 Adhesive fracture states for 200 Vpk sweep**

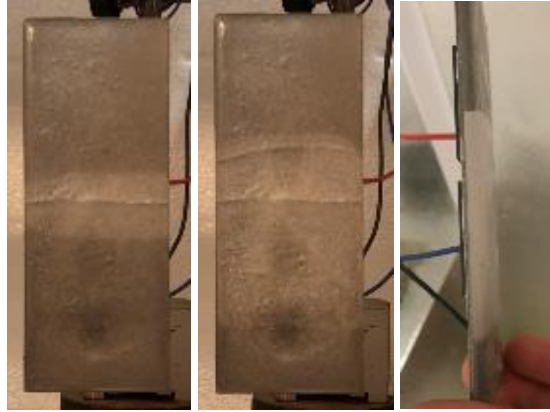


**Figure 31 Adhesive fracture states for 200 Vpk sweep using both ceramics as actuators**

A 3D model of the sample is realized, including ceramics, and removing ice blocs for which the adhesive bond was broken. The modal analysis computation shows that, on the ice surface, there is a high local tensile stress state at the very same position, where the second cohesive fracture started (Figure 31, Figure 32). The initiation on the cohesive crack over a single side can be explained by a small disparity in the ice thickness along the surface. Using previous computation methods and the 3D model of the sample, the power requirements for adhesive fracture propagation are computed (Figure 33). Due to the presence of the ceramics on the structure, the power curve drifts a bit from the power curves computed with the initial 2D model (Figure 33). The 3D computation explains why an instantaneous propagation is observed over a given length and then suddenly stops after reaching 60% of propagation (Figure 31). Indeed, from its descending behavior, the propagation appears to be unstable after 30% of the length. The power become crescent again after 55% of the length.

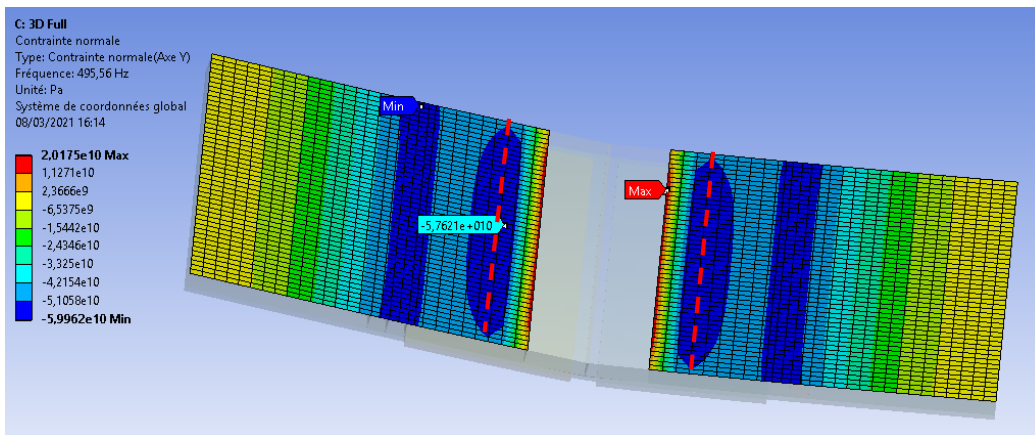


**Figure 32 Finite element normal stress map on the surface of the ice**

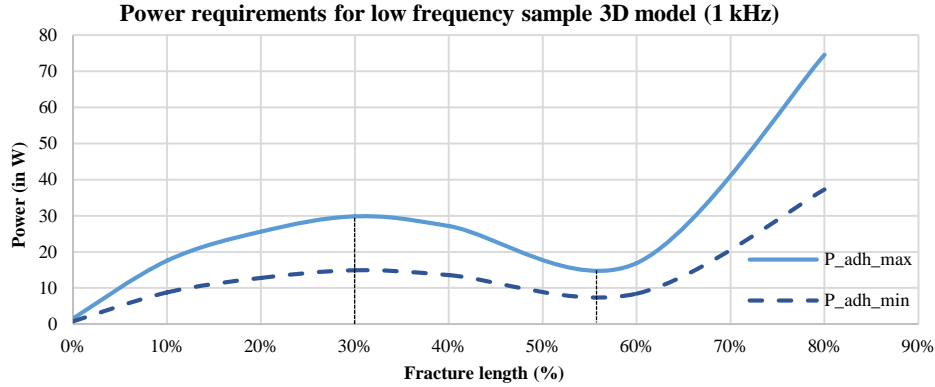


**Figure 33 Power requirements for adhesive fracture propagation with mechanism 1 (3D model)**

As a synthesis of experiments for mechanism 1, it is possible to note that the fracture mechanism has clearly been identified. The cohesive fracture initiation and unstable propagation have been confirmed. The stable behavior of the adhesive crack propagation has also been observed. The experiment highlights the fact that the ceramics are important parts of the structure and they have to be considered when structural computations are made. It also shows that when working with stable crack propagation, it is important to ensure that there are not any other locations where a fracture could be initiated while the stable propagation is being achieved. Test was repeated and similar results were obtained.

### C. High frequency mode – mechanism 2

Sample 2 (Figure 24) is created to fit with the high frequency mode identified thanks to the prelaminar study (Figure 21). Ceramics are placed in a way that each of them is located on an anti-node of the target mode. Doing so, the coupling between actuators and structure is maximized in order to reduce as much as possible the power requirement for the mode actuation. Ceramics are bonded alternating polarization direction so that with the same power supply, one ceramic out of two generates compression while the other ones generate extension, allowing the excitation of such high frequency flexural mode. On each side of the sample, the same combination of ceramics is used to ensure symmetry between the sensor and the actuator and, as for sample n°1, to enable exciting the structure with two sets of actuators.

Since adhesive propagation appears to require a lot of power to occur, an ice thickness of 1 mm is accreted on the sample to reduce as much as possible mechanical power. According to Figure 23, the initiation of the adhesive crack should be observable as the required mechanical power is estimated at 9.0 W. However, if the length of the crack initiated is too small, propagation seems impossible. Thanks to the full 3D model including actuators and sensors, the shear initiation power is estimated at 1.45 W for a shear strength of 1.0 MPa. The power to initiate with tensile stress is also computed and appears to be 3.48 W, with a tensile strength of 3.0 MPa. Using the electromechanical equations given in [8] the voltage and current are computed for both initiations and are under the power supply limit. Therefore, they should be observable. Several sweeps are made increasing gradually the voltage on the actuator. When the input voltage reaches 185 Vpk, voltage drops are observed on the sensor output (Figure 34). Thanks to video recording of the experiment, it is possible to link the drops with cohesive crack appearance (Figure 35).

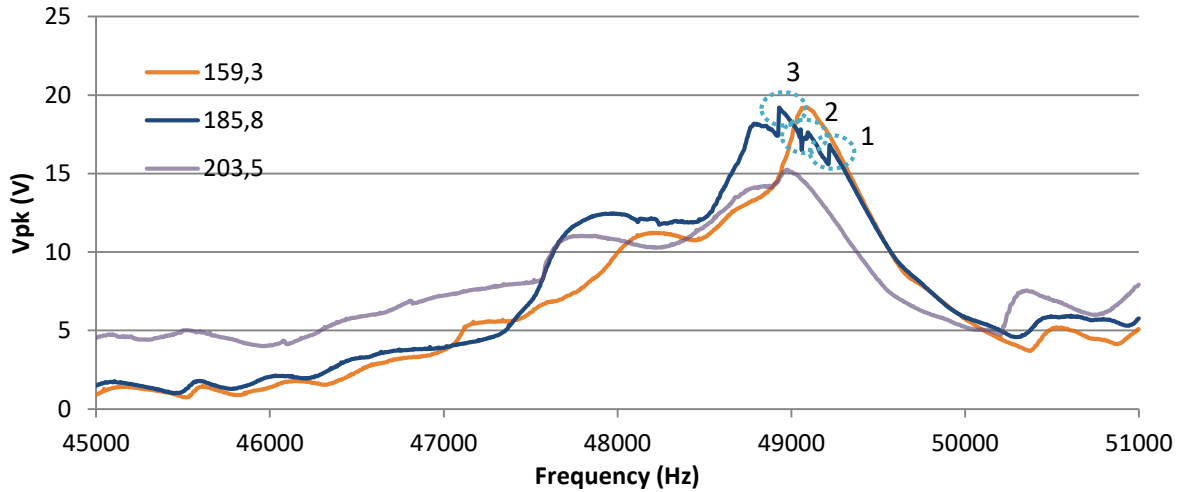


**Figure 34** Sensor output and voltage drops corresponding to fractures

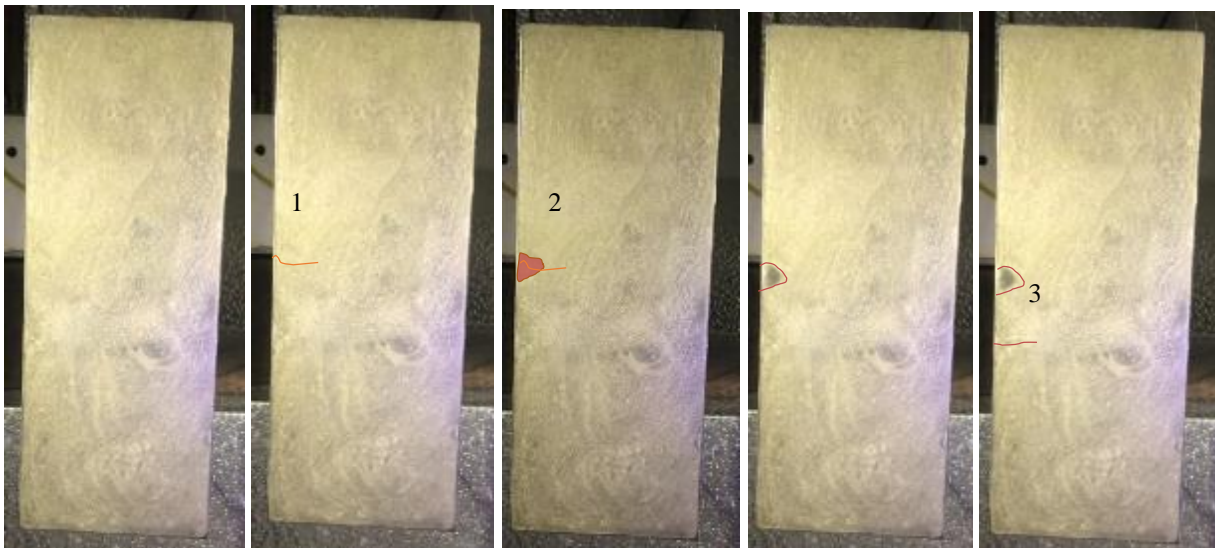


**Figure 35** Fractures states during 185 Vpk+ sweep

The first crack to appear is a small cohesive fracture. A small adhesive fracture is also observed but it seems to correspond to mechanism 1. Finally, a last small cohesive fracture is initiated (Figure 35). A sweep is run with the double actuator configuration and two other cohesive fractures are initiated but there is not any initiation of adhesive fractures to be seen. The unappearance of adhesive initiation can be explained by the fact that the adhesive propagation after the adhesive initiation requires way more power (Figure 23). Therefore, even if adhesive cracks are initiated, the propagation will not happened. It is very likely that the cracks might have been initiated but were impossible to spot with human eye due to their limited length. 3D power computations shows that the power required to initiate cohesive

fracture with this sample is still in range of the power supply limits, and since the power required to initiate with shear stress is lower, it must have happened but was not observable due to the non propagaion of the crack.

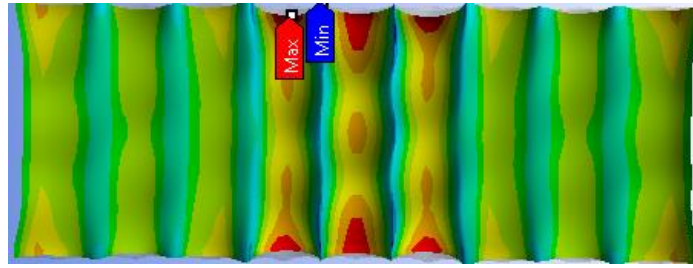


**Figure 36 Tensile stress map on the ice surface for mode of interest**

Tensile stress map obtained from sample 3D modal analysis confirms the position of the cohesive crack initiation (Figure 36) showing that the maximum tensile stress is at the location where the cohesive fracture is observed.

## VIII. Conclusion

This article proposes power criteria and computation methods to enable fast comparisons between various fracture mechanisms for deicing using flexural modes. Power criteria can help computing mechanical power requirements if mechanical properties of the material are known and can be used to assess the power requirements for a given design without having to consider to many mechanical parameters. They can also give indications whether a mechanism can be observed.

Using the criteria to study plates flexural modes existing in the frequency range 100 Hz to 100 kHz, conclusion are drawn on the power requirements to achieve de-icing over the plate. Two mechanisms have been identified and studied. The first mechanism being a tensile dominant mechanism and the second being a shear dominant mechanism. The tensile mechanism occurs at low frequency, lowering the frequency of excitation does lower the power requirement. At higher frequencies, shear initiation becomes possible but the power requirement are much higher. Low frequency flexural modes are better at initiating fractures. After tensile initiation, the cohesive fracture propagates in a unstable way to the ice/substrate interface demanding a relatively low mechanical power input. To realise de-icing, an adhesive crack is then propagated at the interface in a stable way. The power requirement increases as the crack length grows, giving a limited protected area for a limited power. High frequency shear stress modes show unstable crack propagation behavior, however the power requirement is way higher.

This study shows that different axis of improvement can be imagined. Finding a way to extend the protected area using mechanism 1 could be a solution for having an extended low consumption protection system. The optimization of the power criteria according to the geometry of the substrate can be one way. For mechanism 2, as the power consuming part of the mechanism happens to be the early stage of the propagation, finding a way to create a pre-crack of a given length on the right spot could help triggering the unstable crack propagation mechanism and consequently lower the power requirement for a full ice protection.

## References

- [1] R. W. Gent, N. P. Dart, and J. T. Cansdale, 'Aircraft icing', *Philos. Trans. R. Soc. Lond. Ser. Math. Phys. Eng. Sci.*, vol. 358, no. 1776, pp. 2873–2911, Nov. 2000, doi: 10.1098/rsta.2000.0689.
- [2] 'BS 3G 100-2.3.10:1974 - Specification for general requirements for equipment for use in aircraft. All equipment. Environmental conditions. Impact icing'. <https://shop.bsigroup.com/ProductDetail/?pid=00000000000113265> (accessed May 06, 2020).
- [3] 'CS-25 / Amendment 24 | Large Aeroplanes', EASA. <https://www.easa.europa.eu/document-library/certification-specifications/cs-25-amendment-24> (accessed May 06, 2020).
- [4] S. Liscouet-Hanke, 'A model-based methodology for integrated preliminary sizing and analysis of aircraft power system architecture', Oct. 2008.

- [5] S. Ramanathan, V. V. Varadan, and V. K. Varadan, 'Deicing of helicopter blades using piezoelectric actuators', Newport Beach, CA, Jun. 2000, pp. 281–292. doi: 10.1117/12.388906.
- [6] S. V. Venna, Y.-J. Lin, and G. Botura, 'Piezoelectric Transducer Actuated Leading Edge De-Icing with Simultaneous Shear and Impulse Forces', *J. Aircr.*, vol. 44, no. 2, pp. 509–515, Mar. 2007, doi: 10.2514/1.23996.
- [7] J. Palacios, E. Smith, J. Rose, and R. Royer, 'Instantaneous De-Icing of Freezer Ice via Ultrasonic Actuation', *AIAA J.*, vol. 49, no. 6, pp. 1158–1167, Jun. 2011, doi: 10.2514/1.J050143.
- [8] V. Pommier-Budinger *et al.*, 'Electromechanical Resonant Ice Protection Systems: Initiation of Fractures with Piezoelectric Actuators', *AIAA J.*, vol. 56, no. 11, pp. 4400–4411, Nov. 2018, doi: 10.2514/1.J056662.
- [9] E. Villeneuve, C. Volat, and S. Ghinet, 'Numerical and Experimental Investigation of the Design of a Piezoelectric De-Icing System for Small Rotorcraft Part 1/3: Development of a Flat Plate Numerical Model with Experimental Validation', *Aerospace*, vol. 7, no. 5, p. 62, May 2020, doi: 10.3390/aerospace7050062.
- [10] E. Villeneuve, C. Volat, and S. Ghinet, 'Numerical and Experimental Investigation of the Design of a Piezoelectric De-Icing System for Small Rotorcraft Part 2/3: Investigation of Transient Vibration during Frequency Sweeps and Optimal Piezoelectric Actuator Excitation', *Aerospace*, vol. 7, no. 5, p. 49, Apr. 2020, doi: 10.3390/aerospace7050049.
- [11] E. Villeneuve, C. Volat, and S. Ghinet, 'Numerical and Experimental Investigation of the Design of a Piezoelectric De-Icing System for Small Rotorcraft Part 3/3: Numerical Model and Experimental Validation of Vibration-Based De-Icing of a Flat Plate Structure', *Aerospace*, vol. 7, no. 5, p. 54, May 2020, doi: 10.3390/aerospace7050054.
- [12] M. Budinger, V. Pommier-Budinger, A. Reysset, and V. Palanque, 'Electromechanical Resonant Ice Protection Systems: Energetic and Power Considerations', *AIAA J.*, pp. 1–13, May 2021, doi: 10.2514/1.J060008.
- [13] J. Druetz, C. L. Phan, J. L. Laforte, and D. D. Nguyen, 'The Adhesion of Glaze and Rime on Aluminium Electrical Conductors', *Trans. Can. Soc. Mech. Eng.*, vol. 5, no. 4, pp. 215–220, Dec. 1978, doi: 10.1139/tcsme-1978-0033.
- [14] J. Druetz, D. D. Nguyen, and Y. Lavoie, 'Mechanical properties of atmospheric ice', *Cold Reg. Sci. Technol.*, vol. 13, no. 1, pp. 67–74, Oct. 1986, doi: 10.1016/0165-232X(86)90008-X.
- [15] M. Budinger, V. Pommier-Budinger, L. Bennani, P. Rousset, E. Bonaccorso, and F. Dezitter, 'Electromechanical Resonant Ice Protection Systems: Analysis of Fracture Propagation Mechanisms', *AIAA J.*, vol. 56, no. 11, pp. 4412–4422, Nov. 2018, doi: 10.2514/1.J056663.
- [16] H. H. G. Jellinek, 'Adhesive properties of ice', *J. Colloid Sci.*, vol. 14, no. 3, pp. 268–280, Jun. 1959, doi: 10.1016/0095-8522(59)90051-0.
- [17] Z. T. Bieniawski, 'Stability concept of brittle fracture propagation in rock', *Eng. Geol.*, vol. 2, no. 3, pp. 149–162, Dec. 1967, doi: 10.1016/0013-7952(67)90014-2.
- [18] A. Reich, R. Scavuzzo, and M. Chu, 'Survey of mechanical properties of impact ice', presented at the 32nd Aerospace Sciences Meeting and Exhibit, Reno, NV, U.S.A., Jan. 1994. doi: 10.2514/6.1994-712.
- [19] S. Rønneberg, C. Laforte, C. Volat, J. He, and Z. Zhang, 'The effect of ice type on ice adhesion', *AIP Adv.*, vol. 9, no. 5, p. 055304, May 2019, doi: 10.1063/1.5086242.
- [20] E. H. Andrews and N. A. Lockington, 'The cohesive and adhesive strength of ice', *J. Mater. Sci.*, vol. 18, no. 5, pp. 1455–1465, May 1983, doi: 10.1007/BF01111965.